Electrochimica Acta 503 (2024) 144881

Contents lists available at ScienceDirect

Electrochimica Acta

journal homepage: www.journals.elsevier.com/electrochimica-acta

Studies on 3D printing of $Na_3Zr_2Si_2PO_{12}$ ceramic solid electrolyte through Fused Filament Fabrication

Aycan C. Kutlu [a,*], Dorit Nötzel [b], Andreas Hofmann [b], Carlos Ziebert [a], Hans J. Seifert [a], Ijaz U. Mohsin [a]

[a] Institute of Applied Materials – Applied Materials Physics (IAM-AWP), Karlsruhe Institute of Technology, Hermann-von-Helmholtz-Platz 1, 76344 Eggenstein-Leopoldshafen, Germany
[b] Institute for Applied Materials – Materials Science and Engineering (IAM-WK), Karlsruhe Institute of Technology, Hermann-von-Helmholtz-Platz 1, 76344 Eggenstein-Leopoldshafen, Germany

ARTICLE INFO

Keywords:
3D printing
solid-state battery
NASICON
NZSP
Fused Filament Fabrication (FFF)

ABSTRACT

Solid-state batteries are considered being the next step in battery technology to achieve higher energy densities and potentially safer batteries. As there is no organic liquid, the risk of flammability is drastically reduced. Nevertheless, there are numerous challenges associated with the realization of all-solid-state batteries, such as improving slow kinetics, contact interface issues between battery components and cell integration among others. 3D printing holds the potential to address these issues as it allows to improve kinetics by structuring the battery components and the possibility of a customized cell integration. A structured surface of the electrolyte can in principle also enhance interface effects with the metal electrode. To contribute in this regard, composite filaments with $Na_3Zr_2Si_2PO_{12}$ were fabricated and 3D printed. Subsequent sintering of the printed parts after removal of the polymer components led to the required densification of the fully ceramic electrolyte. The parts were microstructurally and electrochemically characterized and showed a reasonable performance with an ionic conductivity of $(3.02 \pm 0.14) \cdot 10^{-4}$ S·cm^{-1} at 20 °C. Critical current density testing revealed stable cycling up to 200 mA·cm^{-2}, with cell failure occurring at a current density of 750 mA·cm^{-2}, demonstrating the application potential of 3D printed full ceramic solid electrolytes.

1. Introduction

Solid-state batteries have received increasing attention in recent years due to their potentially higher safety, higher energy and power density compared to liquid electrolyte based batteries [1]. The eponymous and key component of a solid-state battery is the solid electrolyte (SE). The electrolyte serves as an ion-conducting medium as well as a separator that physically separates the two electrodes of the battery [2]. Various classes of materials exist that can be used as solid electrolyte. A distinction is made between organic and inorganic materials, whereby the inorganic materials can be further subdivided into halides, sulfides, and oxide ceramics. Each of these material classes have their advantages and disadvantages [3,4]. Of particular interest, due to its cathodic, thermal and air stability, are oxide ceramics that have the so-called NaSICON (Na Super Ionic CONductor) structure, which were first described in the 1970s by Hong and Goodenough [5,6]. It is composed of corner-sharing MO_6 octahedra and PO_4 tetrahedra. The composition ($Na_xMM'(PO_4)_3$, where M and M' are metals) allows the diffusion of sodium-ions through a, b and c directions in the crystal structure [7]. The best-known material with this structure is $Na_3Zr_2Si_2PO_{12}$ (NZSP) and it is recognized for its excellent ionic conductivity, which is in the range of 10^{-4} to 10^{-3} S·cm^{-1} at room temperature [8]. NZSP can exist in two space groups depending on its composition. For $Na_{1+x}Zr_2Si_xP_{3-x}O_{12}$ ($0 \leq x \leq 3$) the prevailing space group is $R\bar{3}c$ with exception for $1.8 \leq x \leq 2.2$, where the monoclinic structure C2/c is stable [9]. Typically, ceramic solid electrolytes are produced using conventional powder technology processes. This process involves shaping the material into a green compact by pressing the powder, with or without additives. After a temperature treatment, typically above 1000 °C, during which the powder is sintered, the material acquires its mechanical and functional properties [10–12]. However, the samples produced in the laboratory using this method often exhibit unfavorable geometries for use in real batteries applications, due to high thicknesses of several hundred micrometers to several millimeters. One effective approach to overcome

* Corresponding author.
E-mail address: Aycan.Kutlu@kit.edu (A.C. Kutlu).

https://doi.org/10.1016/j.electacta.2024.144881
Received 19 March 2024; Received in revised form 7 August 2024; Accepted 10 August 2024
Available online 16 August 2024

this issue is the well-established tape-casting process, in which the powder is suspended in a viscous media and subsequently doctor-bladed over a large area [13–15]. This enables very thin layers of just a few μm to be produced. However, due to the two-dimensional limitation of the shapes created, further optimization potential of the solid-state battery is inhibited. Previous work [16] has shown that a structured design of the battery architecture can offer performance advantages. Many methods have been used to enable three-dimensional structuring of batteries, and 3D printing offers an excellent and cost-effective solution for fabricating structured batteries [17]. The trend in 3D printing, especially in Fused Deposition Modeling (FDM)/Fused Filament Fabrication (FFF), is heading towards multi-materials 3D printing, which implies that several materials can be utilized in one 3D print by means of an exchangeable system either via one nozzle or by changing between multiple nozzles [18]. For batteries, this means that various electrode materials, electrolytes and, in principle, even current collectors or housings can be produced in a structured configuration within a single printing process. It has been demonstrated in the literature that structured electrolytes in combination with a metal electrode (e.g. lithium or sodium) can provide an improved performance [19–21].

In the following work, commercial NZSP was used as a filler in a polymeric binder system to produce filaments for 3D printing. Smooth disk-shaped and surface-structured samples were printed, debinded in two stages and finally sintered. The density of sintered samples was determined via Archimedes' principle and the resulting microstructure was analyzed via SEM. Pressed NZSP pellets served as a reference and were sintered the same way. The electrochemical performance of the disk-shaped samples was investigated using Electrochemical Impedance Spectroscopy (EIS), Chronoamperometry (CA), Critical Current Density (CCD) and stripping/plating.

2. Experimental

2.1. Powder characterization

Commercially available $Na_3Zr_2Si_2PO_{12}$ (NZSP, Canrd, China) powder with the NaSICON structure was milled (Pulverisette 7 premium line, Fritsch, Germany) at 700 rpm for various durations of 5, 10, 30 and 60 min, respectively. Two 80 mL zirconia milling jars containing approx. 25 g of powder, 100 g of stabilized zirconia milling beads (2 mm diameter) and approx. 30 g of isopropanol were used for each milling. Milling was carried out for 1 min at a time with a 3-min cooling period. After every 10 min of milling, the milling jars were additionally cooled in a water bath for a few minutes. The particle size distributions of the as-received and milled NZSP powders were determined using a particle size analyzer (LA-950V2, Horiba). The specific surface area of the utilized powders was determined by BET (Gemini VII 2390, Micromeritics Corp., USA) and resulted in 0.26, 2.09, 3.96 and 7.98 $m^2 \cdot g^{-1}$ for the 0, 5, 10 and 60 min milled powders, respectively. The material density of the as-received NZSP powder was determined by Helium-pycnometry (Pycnomatic ATC, Porotec, USA) with a value of 3.21 $g \cdot cm^{-3}$. For further use of the powders, 100 g of powder was milled for each milling duration and then dried at 70 °C overnight. The dried powder was mortared and subsequently sieved using a sieving tower (160 μm, 80 μm) on a vibrator device (Analysette 3 PRO, Fritsch, Germany).

2.2. 3D Printing

The binder system for the feedstocks consisted of polyvinyl butyral (PVB, Mowital B30H, Kuraray GmbH, Germany) as the backbone polymer, polyethylene glycol (PEG, 4000 g mol^{-1}, Carl Roth GmbH, Germany) as the plasticizer and lauric acid (LA, Carl Roth GmbH, Germany) as the dispersant/plasticizer. Several different solid concentrations and binder formulations were produced (see Table 1). The feedstock labels contain details such as the concentration of NZSP in vol%, the duration of the powder milling time in minutes, as well as the volume ratio of the organic components (PVB, PEG, LA) to each other. For example, a label like 55vNZSP60m442 indicates a composition of 55 vol% NZSP, milled for 60 min, with the binder system comprising 40 vol% PVB, 40 vol% PEG and 20 vol% LA. For the feedstock preparation in the internal mixer (W50 EHT, Brabender GmbH, Germany), a suitable quantity of powder was introduced and the lauric acid was added completely to ensure a wetting of the NZSP. The PVB and PEG were then added and the rest of the NZSP was incorporated once the polymers had softened. 45 mL of the mixing chamber had to be filled for proper mixing. The temperature during mixing was 125 °C and the rotation speed of the kneading blades was set to 30 rpm. The duration of mixing was 2 h for all feedstocks and the feedstock that was diluted with additional PEG (45vNZSP5m352*) was mixed for 1 h. The feedstock viscosity in dependence on the shear rate was measured at 160 °C with a capillary rheometer (Rheograph 25, Göttfert, Buchen, Germany). The capillary opening was 1 mm, with a length of 30 mm and an inlet angle of 180 °C. The measured data was corrected with the Weißenberg-Rabinowitsch model. The prepared feedstocks were then subjected to a single screw extruder (Noztek pro HT, Noztek, Shoreham-by-Sea, United Kingdom) in granular form. The extruder nozzle had a diameter of 2.8 mm and filaments were extruded at 100 °C. The filaments were too brittle and hard to be printed off commercial spools, therefore filament rods of 30 - 50 cm were extruded and used for printing. 3D printing was performed on a modified "X350 pro" printer (German RepRap, Feldkirchen, Germany). The 3D models were created using a CAD software (Autodesk fusion 360, Autodesk Inc. USA). A diameter of 11.8 mm and a height of 2.0 mm were used for the plain disk-shaped samples (see S 1a)). The same dimensions were used for the structured samples, however, the edge (diameter 0.6 mm) had a height of 0.5 mm and the structure lines had a thickness of 1.2 mm and height of 0.3 mm (see S 1b)). The slicer software Ultimaker Cura (Ultimaker, Netherlands) was used to configure the printing parameters for the created 3D models. A hardened steel nozzle with a diameter of 0.6 mm was used and the extrusion width (*line width* in slicer) of the deposited layer was set to 0.6 mm accordingly. The layer height was set to 100 μm, but modified in the generated *gcode* to 90 μm to achieve a better interface healing between subsequent deposited layers. To avoid typical elongated voids in between deposited material tracks in 3D printing, the *infill density* was set to 105 % which fills up voids. The *printing direction* was turned by 90 ° after each layer. The *printing temperature* was 160 °C without *part cooling* and the *printing bed temperature* was set to 45 °C. The printing substrate was an adhesive polypropylene-tape (solid&strong, tesa SE, Norderstedt, Deutschland) to ensure good adhesion to the printing bed. *Printing speed* was set to 5 $mm \cdot s^{-1}$.

Table 1
Different compositions of prepared feedstocks.

Material & content (vol%)	55vNZSP 60m442	55vNZSP 10m442	50vNZSP 5m442	50vNZSP 5m352	45vNZSP 5m352*
NZSP ($t_{milling}$)	55 (60 min)	55 (10 min)	50 (5 min)	50 (5 min)	45 (5 min)
PVB	40	40	40	30	33
PEG	40	40	40	50	51
LA	20	20	20	20	16

2.3. Postprocessing

The 3D prints were first debinded in demineralized water for 24 h at room temperature. After drying, the parts were thermally debinded with a slow heating rate of 0.5 $K \cdot min^{-1}$ up to 500 °C with several intermediate dwell times of 2 h in a debinding furnace (HT6/28, Carbolite Gero GmbH & Co. KG, Germany). The debinded parts were sintered in a muffle furnace (RHF 17/3, Carbolite Gero GmbH & Co. KG, Germany) with a heating rate of 2 $K \cdot min^{-1}$ up to 500 °C and from then on with 5 $K \cdot min^{-1}$ up to 1230 °C with a dwell time of 5 h pressureless in air. Microstructure investigations were performed on cross-sections of

sintered pellets which were first hand grinded with 800, 1000, 2500 and 4000 sandpaper grits and then polished subsequently with 3 and 1 μm diamond suspensions. The polished samples were thermally etched at 1100 °C for 30 min with a temperature rate of 10 K·min^{-1}. A thin sputtered gold coating on the polished surface was used to make the sample conductive for SEM (XL 30 S, Philips, Netherlands) imaging. The same procedure was repeated for reference samples where the powder was first pressed uniaxially (10 mm diameter) with approx. 375 MPa for 3 min and then cold isostatically (KIP 300 E, Paul-Otto Weber GmbH, Germany) at 500 MPa for 6 min. At least 800 grains were measured via the software ImageJ to determine the grain size distribution for each material type. The chemical analysis was done using a carbon-sulfur analyzer (LECO—CS, LECO Corp., USA) for the carbon content, thermal extraction with carrier gas (LECO—ON, LECO Corp., USA) for the oxygen content and ICP-OES (OPTIMA 4300 DV, PerkinElmer, USA) for the other elements.

2.4. Electrochemical measurements

Electrochemical impedance spectroscopy was performed on 1230 °C / 5 h sintered specimens that were fine grinded up to 4000 sandpaper grit and sputtered with gold on both sides (25 mA, 120 s, Sputter Coater, Structure Probe Inc., USA). The excitation voltage for the EIS measurement was 50 mV and was conducted in a temperature range from 80 to −140 °C under flowing nitrogen gas using an analyzer (NEISYS, Novocontrol Technologies, Germany) in the frequency range between 10 MHz and 100 mHz. The same samples from the impedance measurements were also used for the CA measurement. The samples were placed in special battery holders (BH-1i, Biologic, France) and measured using a Biologic VMP3. A constant voltage of 0.5 V was applied for 6 h at 25 °C and the progression of current over time was measured to estimate the electronic conductivity.

The performance of the 3D printed sintered electrolytes was investigated using the CCD and stripping/plating method. The samples were successively ground up to 4000 grit sandpaper and dried at least overnight in an oven inside the glovebox (UNIlab pro, MBraun, Germany) with <0.1 ppm H_2O and <0.1 ppm O_2 at 120 °C in a vacuum of 10^{-3} bar. A piece of sodium metal was cut from a block using a scalpel and oxidized areas were removed. The piece of sodium was rolled as flat as possible between plastic foils with a roller and punched out. The punched sodium disks were pressed onto the ceramic electrolyte using a uniaxial press (MSK-110, MTI Corp., USA) at 1000 psi (about 6.9 MPa) for 5 min. The symmetrical pressed prepared electrolytes were inserted into a spring-loaded cell (TSC Battery, rhd instruments, Germany) and cycled in a climate chamber at 25 °C using CCD and stripping/plating. For the CCD test, the current density was increased successively, keeping the quantity of charge constant by reducing the half-cycle time accordingly with increasing current density. For stripping/plating, the first 10 cycles were cycled at 50 μAh·cm^{-2} and then continued with 100 μAh·cm^{-2}.

3. Results

3.1. 3D Printing of the ceramic solid electrolyte NZSP

Various fine milled NZSP powders were prepared and used to produce several different feedstocks. The best processable feedstock was used for 3D printing of flat-disk shaped and structured samples. The printed samples were evaluated with regard to their sintered quality (density and microstructure) and compared to conventionally produced samples. Electrochemical tests were performed on the printed samples to demonstrate their suitability for the use in all-solid-state batteries.

As received, the NZSP powder showed a coarse particle size distribution with a median particle size of 110 μm. SEM images in S 2 reveal that a significant portion of these large particles are aggregates. Since the coarse powders are impractical for processing with both 3D printer, and pressing methods, the powder was milled at 700 rpm for various durations as illustrated in Fig. 1a. First, the powder was milled for 60 min in order to obtain a very fine and sinter-active powder. In addition, the milling duration was gradually reduced to obtain coarser particles, which influences the processing properties (e.g. viscosity) for the feedstock development. It is apparent that there is consistently a bimodal size distribution after milling, whereby the frequency of small particle sizes increases with increasing milling duration. The frequency of coarser particles decreases accordingly. The median particle size shows a gradual reduction of the particle diameter with the duration of milling, whereas the D90 value for the milled powders remains almost constant from a milling duration of at least 10 min. This implies that a part of the coarser fraction consists of agglomerates. The effect of the milling duration and the corresponding reduction in the size of the powder particles can also be seen in the specific surface area of the powders shown in Fig. 1b. Just as the median particle size decreases with increasing milling duration, the specific surface area of the powder consequently increases.

Feedstocks with varying compositions of polyvinyl butyral (PVB), polyethylene glycol (PEG), lauric acid (LA) and NZSP powder milled for different durations were produced (cf. Table 1). The internal mixer used to prepare the feedstocks records the torque that is applied during the mixing process, which is necessary to maintain the rotational speed of the mixing blades at 30 rpm. The development of the torque over time is shown in Fig. 1c. It is apparent that the powder milled for 60 min leads to a significantly higher torque due to its higher specific surface area of approx. 8 m^2·g^{-1}, which can also be seen from the fact that it took significantly longer to fill in the powder (visible by the several peaks). In contrast, the powder milled for 10 min has a reduced final torque due to the coarser powder with half the specific surface area of approx. 4 m^2·g^{-1}. A main reason why feedstocks containing coarser powders are easier to process at higher fill levels than fine powders is, that the specific surface area greatly influences the critical fill level [20]. Since the kneading behavior correlates with the viscosity of the feedstock, assumptions can be made about the processability. It has been observed in a previous study [16], that feedstocks with final torques <10 Nm are more likely to successful printing. Therefore, the milling duration was further reduced to obtain a coarser powder, leading to a reduction in viscosity and thereby the recorded torque. Moreover, a lower solid content of 50 vol% likewise ensures a decrease in the viscosity of the feedstock. The resulting mixing curve shows a final torque of 8.13 Nm and further attempts to make the binder system "softer" by increasing the ratio of PEG to PVB (1:1 to 5:3) resulted in a final torque of 7.53 Nm (see Fig. 1c) with the same NZSP concentration. In general, a filament should fulfill three important requirements in order to be processable for a standard FFF 3D printer: 1. the hardness of the filament may not be too hard, as this would prevent the extruder gears from penetrating the material and conveying the filament, but at the same time it shouldn't be too soft, as this would cause the filament to be squeezed under the pressure of the extruder gears. 2. the filament shouldn't be too brittle, else it might break in the extruder and it should have at least a modest elasticity so that deformation of the filament doesn't lead to rupture. 3. the viscosity of the feedstock must be low enough so that it melts quickly inside the printing nozzle and can be extruded, however, at the same time the viscosity should not be too low so that the deposited strands retain the desired shape [21]. As the feedstocks could be processed into filaments but were not printable due to the aforementioned filament properties, an additional amount of PEG was added to the feedstock 50vol%NZSP-5min-352 indicated by the green arrow in Fig. 1c. The additional PEG softens the filament and reduces the viscosity, resulting in a reduced solid content of 45 vol% (45vol%NZSP-5min-352*) and a final torque of 2.60 Nm. Despite the different compositions of the feedstocks, there is a strong tendency towards increasing torque with increasing solid content, as shown Fig. 1d. The torque shows the approach of an exponential progression with increasing ceramic concentration, which suggests that the feedstock compositions are close to

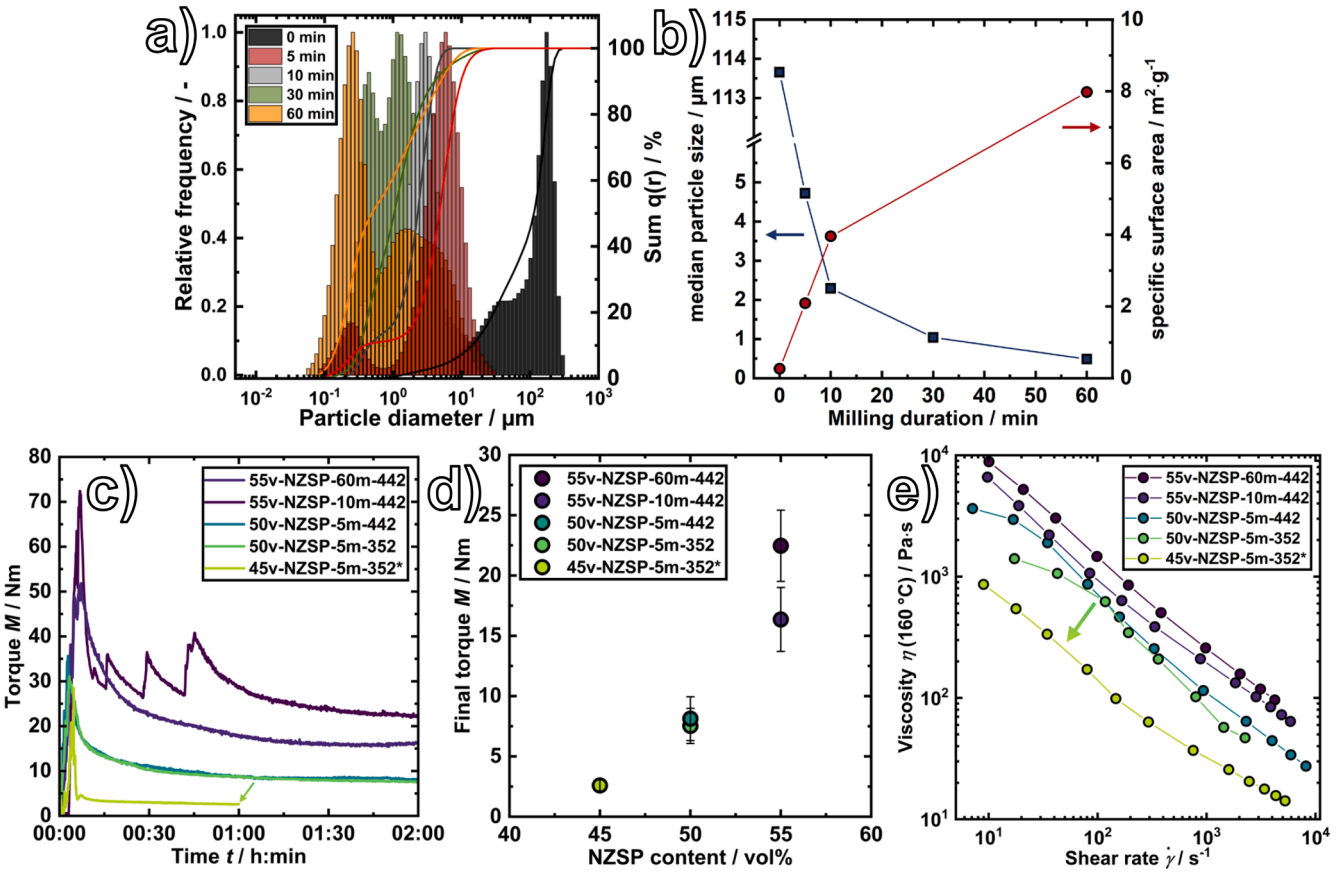

Fig. 1. Feedstock and feedstock component characteristics. a) Particle size distrubtion of different milling durations of NZSP powder. b) Median particle size and specific surface area of the differently milled NZSP powders with milling duration. c) Mixing behavior of the prepared feedstocks. d) Torque values at the end of the mixing process of different NZSP concentrated feedstocks. e) Viscosity at 160 °C against the shear rate for the prepared feedstocks.

the critical powder concentration [22]. The tendencies observed in the torque curves of the different feedstocks are reflected accordingly in their shear rate-dependent viscosity, shown in Fig. 1e at 160 °C. All feedstocks show a shear thinning behavior which is typical for filled polymer systems [23]. The feedstocks with coarser powders have, as expected, lower viscosities due to a smaller specific surface area, thereby less interfacial area between polymer and ceramic. Furthermore, the viscosity is tremendously lowered by a reduced solid content and a higher amount of PEG as the 45v-NZSP-5m-352* had the lowest viscosity by far. The filaments prepared using the different non-diluted feedstocks tended to be too hard, along with their high viscosity, so that filament grinding occurred at the extruder and the filament could not be fed to the heated nozzle with sufficient force [24].

Diluting the feedstock with PEG lowers the hardness and viscosity sufficiently for 3D printing. Nonetheless, the reduced amount of ceramic in the diluted feedstock causes a lower green density of the part. The term “green density” refers to the density of the ceramic portion of the fabricated part before the sintering step and is an important parameter which influences the sintering behavior. To improve the bulk density of the sample, i.e. avoid typical 3D printing artifacts such as elongated voids along printed tracks, the generated gcode after slicing the 3D model was modified and the z-layer height was reduced by 10 µm per layer. These voids are typically process-related defects in the form of elongated cavities during 3D printing. Due to this problem, the performance of printed objects is often inferior in comparison to conventional manufacturing methods [25]. The 3D printed parts were debinded in demineralized water for 24 h and dried afterwards. Disk-shaped specimen had a mass loss of (20.71 ± 2.13) % and the structured specimen of (23.12 ± 0.62) %. Solvent debinding creates an open porosity in the fabricated component. The formed channels allow the extraction of gaseous species produced during thermal debinding without causing the parts to swell [26]. With thermal debinding the disk-shaped specimen lost another approx. 15 % of mass, while the structured specimen only lost about 10 %. The higher mass loss in the solvent debinding of the structured specimens is due to the higher surface area to volume ratio, whereby the diffusion paths for the PEG to the water, outside of the part, are shorter [26]. The fact that the mass loss was respectively higher in the thermal debinding and lower in the liquid debinding for the disk-shaped specimens suggests that not all of the PEG was removed within the 24 h solution debinding.

3.2. Sintering and microstructure

3.2.1. Sintering

Fully debinded 3D printed samples sintered at 1230 °C for 5 h were compared to pressed reference samples that were sintered the same way. Due to the very high green density of the pressed samples with (73.05 ± 0.64) %, high relative sintering densities of (97.60 ± 0.12) % were obtained by considering a theoretical density of 3.27 g·cm^{-3} for NZSP, comparable to literature values for relative densities of 96 - 98 % [27–29]. Since the printable feedstock contains a moderate ceramic concentration of 45 vol%, a significantly lower green density of the completely debinded part is produced, thus strongly influencing the sintering kinetics, resulting in a substantially lower sintered relative density of (86.70 ± 1.07) %. The difference in the sintering behavior of pressed material and feedstock material is further described in S 3 (Supporting Information).

3.2.2. Microstructure

SEM images in Fig. 2 show the microstructure of the two sintered

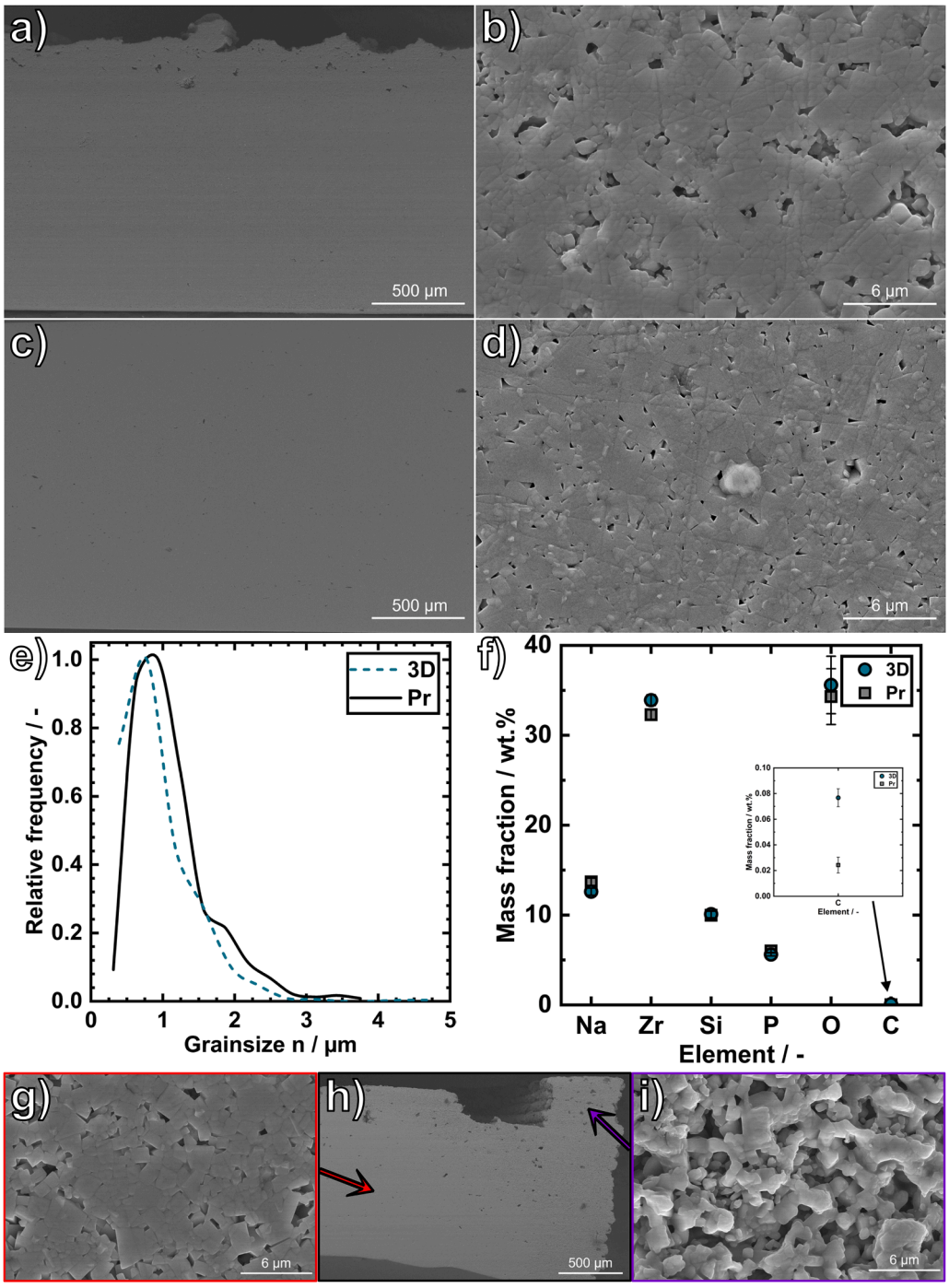

Fig. 2. Comparison of pressed NZSP and 3D printed NZSP post sintering. a) and b) 3D printed sample cross section at magnifications of 50x and 4000x, respectively. c) and d) pressed sample cross section at magnifications of 50x and 4000x, respectively. e) Grain size distribution after sintering at 1230 °C for 5 h of 3D printed (3D) and pressed (Pr) samples. f) Chemical composition after sintering. g) Dense region of a 3D printed, structured and sintered pellet at a magnification of 4000x, h) overview of the 3D printed and structured pellet's cross section at a magnification of 50x and i) porous region within the surface structure with a magnification of 4000x.

samples, pressed and printed, respectively. Both samples show relatively homogeneous microstructures. However, larger pores can be seen in the upper area of the printed sample in Fig. 2a. Furthermore, the higher magnification in b reveals that the NZSP grains are well interconnected. However, there is still fine isolated porosity which is responsible for the lower relative sintered density of the printed NZSP. This also reveals that sufficient open porosity was created during solvent debinding, ensuring that the parts did not swell during thermal debinding. In contrast, a few large pores can be seen in the overview (see Fig. 2c) of the pressed sample. These pores might be caused either by initial pressing artifacts or possibly by the formation of volatile species (P_2O_5, Na_2O) during sintering [30]. The higher magnification shows a significantly denser and more homogeneous microstructure. The grain size distribution displayed in Fig. 2e, exhibits that the 3D printed sintered sample has a narrow distribution with the most common grain size of about 0.73 µm and a shoulder at larger grain sizes of >1.5 µm. The conventionally prepared NZSP has a slightly shifted distribution towards larger grain sizes, with the most frequent grain size being around 0.85 µm. The

pressed sample also has a shoulder at grain sizes >1.6 μm. The observed trend can also be seen in the median grain size, which is (0.58 ± 0.37) μm for the 3D sample and (0.83 ± 0.40) μm for the pressed sample. As a result of the broad size distribution, the average grain sizes are moderately larger at (0.96 ± 0.40) μm for pressed- and (0.72 ± 0.37) μm for printed material. These grain sizes are comparable with values found in literature when sintered at similar temperatures [31,32]. The enhanced grain growth of the pressed sample is due to the sintering mechanism, which is a diffusion-controlled materials transport [33]. Since the pressed sample had a very high green density, the individual grains already have significantly more grain-grain contact zones compared to the printed samples with a significantly lower green density. The higher contact area between the grains supports the material transport while sintering, so that an enhanced densification is realized (see S 3). Due to the improved sintering and resulting high sintered density, the densification enters the third sintering phase where grain growth takes place and the microstructure develops [33].

Chemical analysis was carried out to investigate the differences in composition due to the different sintering characteristics and associated densification of pressed and printed NZSP, and the fact that phosphorus and sodium composites are known to evaporate over time at high temperatures in NZSP (see Fig. 2f). The printed sintered samples sodium concentration is around 1 wt% less than the reference. This might be due to the open-channel porosity, which allows volatile components to evaporate from within the volume during the sintering process. This is also supported by the fact that there are fewer large pores in the volume of the printed part than in the pressed sample, meaning that volatile species can not be released. Interestingly, the inset of Fig. 2f confirms that the residual carbon content of the printed material is about 3 times higher compared to the reference, despite the high temperatures of 1230 °C in normal air atmosphere. Valera-Jiménez et al. [34] showed on FFF printed full ceramic electrode materials that a conductive carbon coating had formed around the grains after a heat treatment. However, the temperature of 900 °C was significantly lower than in the present work. Nevertheless, the total amount is negligible to have any effect on the functional properties as perceived by the comparable electronic conductivity from the CA measurement, which will be discussed in Section 3.3.2.

The working principle of 3D printing, in which a component is built up line by line and layer by layer, makes it possible to create various three-dimensional structures [35]. To take advantage of this method regarding the electrolyte, a complex geometry with a track-shaped surface structure was printed and processed. However, due to the moderate ceramic concentration in the feedstock, an inhomogeneous sintering behavior of the structured part can be observed as displayed in Fig. 2g-i. Voluminous sections tend to densify more than narrower sections, which leads to a distortion of the part (see Fig. 2g). One of the reasons for this is the uneven shrinkage due to local concentration differences [36]. A comparable microstructure to the disk-shaped samples can be seen in the highly densified areas, while in the narrower structures only a skeletonization has occurred (see Fig. 2i). For the printing and successful sintering of structured samples, the green density, i.e. the ceramic content of the feedstock, must be increased in order to achieve a more even powder distribution in the part and thus an improved sintering behavior [37]. However, the complexity of the interaction between powder type, particle size, particle size distribution, particle morphology and the interaction between the type and proportion of backbone polymer, plasticizing polymer and dispersant must be considered in the feedstock development [38]. Due to the large number of parameters and the required amount of powder (about 70–90 g ceramic powder), making these considerations is even more challenging.

3.3. Electrochemical performance

3.3.1. Ionic conductivity

The electrochemical properties of the electrolytes produced were investigated using electrochemical impedance spectroscopy (EIS). Fig. 3a shows the calculated conductivities σ_{ionic} of the EIS data in the Ahrrenius illustration, as well as the activation energies E_a calculated using the slope of the linear fits and Eqs. (1) and (2).

$$\sigma_{ionic} = \frac{h}{A \cdot R} \tag{1}$$

$$\sigma_{ionic} \cdot T = \sigma_0 \cdot e^{-\left(\frac{E_a}{k \cdot T}\right)} \tag{2}$$

With h sample thickness, A area, R resistance, T temperature, σ_0 pre-exponentional factor and the Boltzmann constant k. The total conductivity of the 3D printed sample is clearly inferior to that of the pressed sample. The conventional sample has a conductivity of $(8.89 \pm 0.16) \cdot 10^{-4}$ S·cm^{-1} while the printed sample exhibits a conductivity of $(3.02 \pm 0.14) \cdot 10^{-4}$ S·cm^{-1} at 20 °C. The values for the pressed sample are slightly higher than many reported conductivities in the literature and the printed samples are in the same order as the literature data for NZSP ($x = 2.0$) [28,29,39,40]. There is a wide range of activation energies reported in literature and the electrolytes produced in this study are within this range [29,40–42]. The reason for the significantly differing conductivity and $E_{a-grain}$ can be attributed to several factors. 1) One of the causes is the disparity in the relative density of the printed and pressed material after sintering, which is also discussed further in the supplementary information (see Seq 1). This has a remarkable impact on the conductivity, since ion transport within a solid material occurs through a hopping mechanism. The lower density is also accompanied by a smaller grain-to-grain contact area, which makes the transportation of sodium-ions more difficult between grains. An increase of the ceramic concentration in the feedstock improves the sintering behavior, which allows 3D printed functional ceramics to achieve equivalent properties to those of conventionally produced ceramics [16]. (2) As discussed in Section 3.2.2, the printed sample has less sodium in its structure after sintering and thus a lower concentration of charge carriers, and as a result the total conductivity is lower. This also explains why the grain conductivity of the printed sample in particular is lower than that of the pressed sample. This can also be seen in the Nyquist plots (see S 4) by the width of the first semicircle, which is significantly smaller than that of the printed sample and has a higher apex frequency indicating that the grain conduction process is faster.

3.3.2. Electronic conductivity

CA measurements were performed to ensure that the contribution to the conductivity measured in the EIS results is mainly due to sodium-ion movement. Fig. 3b shows the polarization measurements of the printed and pressed sample, where a constant voltage of 0.5 V is applied and the resulting current flow is measured over time. Blocking electrodes (sputtered gold) prevent the transfer of Na^+-ions and only allow the flow of electrons during polarization. The electronic conductivity can then be estimated by the established steady-state current using Eq. (3).

$$\sigma_{el} = \frac{h \cdot I}{A \cdot U} \tag{3}$$

where I is the current and U the applied voltage. It can be seen that for both sample types a negligible low electronic conductivity of about $1 \cdot 10^{-8}$ S·cm^{-1} can be determined and thus the calculated ionic conductivity indeed refers to purely ionic charge transfer. Consequently, a high transference number of almost 1, which is usual for oxide ceramics [28,43,44], can be deduced. With a transference number approaching 1, the tendency to self-discharge through the electrolyte is suppressed, allowing the stored charge to be kept for a longer period of time, as well as reducing parasitic reactions due to electron leakage.

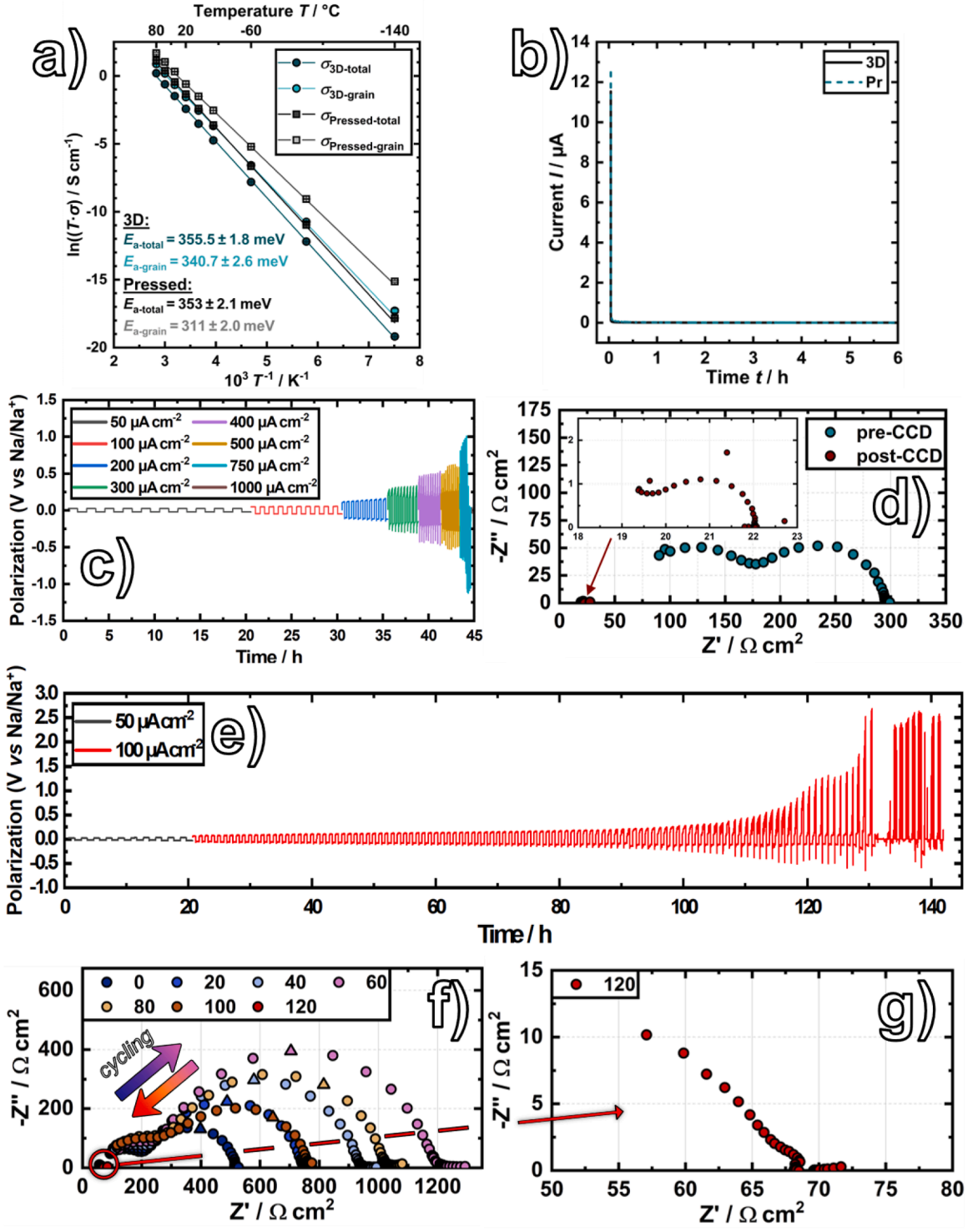

Fig. 3. Electrochemical measurements. a) Ahrrenius plot of the impedance data for printed and pressed NZSP. b) Pressed and 3D printed DC polarization. c) CCD of 3D printed NZSP at various current densities. d) EIS before and after the CCD. e) Stripping/Plating of 3D printed NZSP. f) Resistance evolution with stripping/plating. The triangular symbols at the apex of the second semicircles indicate a frequency of 1930 Hz.The arrows with color gradient show that the impedance increases up to 60 cycles and decreases thereafter. g) Enlarged Nyquist plot of the EIS measurement after short circuit at 120 cycles.

3.3.3. Critical current density & stripping/plating

Critical current density (CCD) tests were performed on symmetrical Na|3D-SE|Na cells to identify the maximum current density at which the cell can be cycled without premature failure. There are several approaches of conducting CCD tests that can be used to investigate specific properties of the material or cell (e.g. interface) [45,46]. In this work, the transferred capacity was kept constant, which implies that the duration per half cycle is reduced with increasing current density. For each current density step, 10 cycles were run starting with 0.05 $\mu A \cdot cm^{-2}$ ($t = 1$ h per half cycle) up to 1 $mA \cdot cm^{-2}$. Fig. 3c shows that stable cycling is possible up to 200 $\mu A \cdot cm^{-2}$ and that various effects emerge at higher currents. Finally, the cell is fully short-circuited at the current density of 750 $mA \cdot cm^{-2}$, which can be seen from the polarization drop and additionally in the impedance measurements shown in Fig. 3d. The

inset displays the impedance after the short-circuit of the CCD. Oh et al. [47]. found similar values for $Na_3Zr_2Si_2PO_{12}$ of CCDs, suggesting that the interface between electrolyte and electrode has a significant influence on the value of the CCD. Heat treatments to remove impurities on the surfaces of the SE indicated that higher CCD values can be achieved for heat treated SE surfaces [47]. The impedance spectra in Fig. 3d also indicate an initially high impedance with two clearly depicted semicircles. The second semicircle describes the interfacial resistance of the two sodium electrodes to the solid electrolyte. This reveals that despite the applied pressure of about 1000 psi (about 6.9 MPa) during cell production, a sufficiently good interface between SE and Na could not be established. Studies on the interface while cycling have shown that the resistance is strongly dependent on the contact area of the metal electrodes with the solid electrolyte. Subsequent cycling can additionally lead to dewetting of the metal electrodes, decreasing the contact area further, thus to an increase in resistance which results in failure of the cell [48,49]. However, the issue of the non-ideal interface between electrolyte and alkali metal is known for oxide solid-state electrolytes and is a frequent reason for premature failure of cyclization [50]. Nevertheless, it was possible to cycle the cell successfully with current densities commonly found in the literature owing to the good ionic conductivity of the NZSP material. The inset in Fig. 3d shows the impedance after the short circuit and thus the termination of the CCD, which can be seen from the significantly lower resistance. It can be expected that a further optimization of the interface properties of the SE, facilitating an improved wetting behavior with sodium, will lead to a substantial increase in performance and thus allow significantly higher current densities, as shown by Ma et al. [51]. The group achieved a CCD of 14 $mA{\cdot}cm^{-2}$ by preparing a NZSP pellet with a polymeric coating at the edges to prevent dendrites on the surface and applying a high stack pressure. However, this approach is quite time-consuming, requiring successive coating and drying of several layers of polymer at the edges.

Stripping/plating was performed to investigate the cycling stability of the 3D printed/sintered material as shown in Fig. 3e. Initially, 10 cycles were performed with 50 $\mu A{\cdot}cm^{-2}$ to ensure a slow and potentially better sodium deposition on the electrolyte interfaces. As expected based on the CCD, the first cycles are stable, although an increasing polarization can be observed. The progression of the polarization is fairly asymmetrical, which is an indication of pore formation at the interface of one electrode [45,52]. Fig. 3f shows an EIS measurement every 20 cycles from the beginning of the applied current density of 100 $\mu A{\cdot}cm^{-2}$, which allows an understanding on which process is primarily responsible for eventual effects. Even the first EIS measurement before applying the increased current density shows a resistance of about 520 $\Omega{\cdot}cm^2$. More than half of this resistance can be attributed to the two interfaces (second semicircle) between the sodium metal electrodes and the electrolyte. The insufficient wetting of the ceramic with the sodium leads to an increasingly uneven stripping and plating, as the sodium electrodes tend to be connected to the electrolyte in a point-like manner. As the number of cycles increases, the interface deteriorates and the resistance of the cell also increases. At a certain point, the resistance decreases (after about 80 cycles), which can be recognized by voltage peaks and a sudden drop in polarization. This behavior indicates a high probability of dendrite growth through the microstructure of the ceramic due to point like contact points between sodium and SE [53]. The progression of sodium dendrites reduces the distance between the two electrodes, thus results in a decrease of the total resistance. As the process continues, this effect becomes more pronounced until a short circuit occurs after around 120 cycles, identifiable by the small impedance visible in Fig. 3g. CCD as well as the stripping/plating behavior show that the material itself performs excellently. Though, the cell design needs further considerations and optimizations in order to overcome the shortcomings, particularly the interface between sodium and SE. Detailed studies by Ortmann et al. [54] on the interface between $Na_{3.4}Zr_2Si_{2.4}P_{0.6}O_{12}$ and sodium metal showed the relation between an increased applied stack pressure and a reduction in interfacial impedance. Another aspect of the study involved the anodic dissolution of sodium in a symmetric cell without an active stack pressure demonstrating an increase in interfacial impedance and is explained by pore formation reducing the contact between sodium metal and the ceramic electrolyte, which was observed by means of FIB-SEM cross-sections of the interface. This underlines the challenge of the cell design with regard to the limitations imposed by the interface between the metal electrode and the solid electrolyte, which has also been identified as a bottleneck in this work.

4. Conclusions and outlook

This work comprehensively addressed the fabrication of processable feedstock for the production of functional 3D printed solid electrolytes. The all-ceramic electrolytes were analyzed from the microstructure to the electrochemical performance. During this study, a moderately concentrated feedstock (45 vol%) was optimized to low viscosities and processed by means of a FFF 3D printer and was then thermally post-processed. The electrochemical characterization of the printed material showed a good ionic conductivity of $(3.02 \pm 0.14) \cdot 10^{-4}$ $S{\cdot}cm^{-1}$ at 20 °C, despite its moderate relative density. Carbon residues which remained after the temperature treatments were negligible and had no detrimental effect on the conduction and cycling properties. The CCD and stripping/plating tests demonstrated the favorable performance of the material, as well as the functionality of the printed electrolytes. Although they also revealed that greater efforts need to be devoted to the cell design, as the causes of failure were located at the interfaces between the two sodium electrodes and the solid-state electrolyte due to the poor wetting of sodium with NZSP. 3D printing also enables the realization of various structures, however, the example of a surface structured sample shown in this work has disclosed that a highly concentrated feedstock is essential, especially for structured parts, in order to keep the shrinkage as low as possible and to ensure a homogeneous densification/contour accuracy.

Further in-depth investigation into the fabrication of composite feedstock materials for 3D printing of NZSP solid electrolytes, in conjunction with electrode materials, is essential for the production of all-solid-state batteries. This study is in progress and will consider several critical aspects such as co-sintering, thermodynamic stability, effective densification and ensuring sufficient mechanical strength of the battery components.

CRediT authorship contribution statement

Aycan C. Kutlu: Writing – review & editing, Writing – original draft, Visualization, Validation, Methodology, Investigation, Formal analysis, Conceptualization. **Dorit Nötzel:** Writing – review & editing, Validation, Supervision, Methodology. **Andreas Hofmann:** Writing – review & editing, Visualization, Validation, Supervision, Funding acquisition. **Carlos Ziebert:** Writing – review & editing, Resources. **Hans J. Seifert:** Writing – review & editing, Validation, Supervision, Resources. **Ijaz U. Mohsin:** Writing – review & editing, Visualization, Validation, Supervision, Resources, Project administration, Funding acquisition.

Declaration of competing interest

The authors declare the following financial interests/personal relationships which may be considered as potential competing interests:

Aycan C. Kutlu reports financial support was provided by German Research Foundation. If there are other authors, they declare that they have no known competing financial interests or personal relationships that could have appeared to influence the work reported in this paper.

Data availability

The raw data of relevant measurements is available in Zenodo for

open access at DOI: 10.5281/zenodo.13253922.

Acknowledgements

This work contributes to the research performed at CELEST (Center for Electrochemical Energy Storage Ulm-Karlsruhe) and was funded by the German Research Foundation (DFG) under Project ID 390874152 (POLiS Cluster of Excellence, EXC 2154). In addition, Ms. Offermann and Ms. Raab are thanked for the powder characterization. Further the group Chemische Analytik (IAM-AWP) led by Dr. Bergfeldt is thanked for the chemical analysis of the powders.

Supplementary materials

Supplementary material associated with this article can be found, in the online version, at doi:10.1016/j.electacta.2024.144881.

References

[1] J. Janek, W.G. Zeier, Nat. Energy 1 (2016), https://doi.org/10.1038/nenergy.2016.141.
[2] W. Hou, X. Guo, X. Shen, K. Amine, H. Yu, J. Lu, Nano Energy 52 (2018) 279–291.
[3] P. Ganesan, M. Soans, M.A. Cambaz, R. Zimmermanns, R. Gond, S. Fuchs, Y. Hu, S. Baumgart, M. Sotoudeh, D. Stepien, H. Stein, A. Groß, D. Bresser, A. Varzi, M. Fichtner, ACS Appl. Mater. Interfaces 15 (2023) 38391–38402.
[4] Z. Yang, B. Tang, Z. Xie, Z. Zhou, *ChemElectroChem* 2021, 8, 1035–1047.
[5] J.B. Goodenough, H.Y.-P. Hong, J.A. Kafalas, Mater. Res. Bull. 11 (1976) 203–220.
[6] C. Li, R. Li, K. Liu, R. Si, Z. Zhang, Y. Hu, Interdiscipl. Mater. 1 (2022) 396–416.
[7] M. Avdeev, Chem. Mater. 33 (2021) 7620–7632.
[8] Q. Ma, F. Tietz, *ChemElectroChem* 2020, 7, 2693–2713.
[9] M. Guin, *Chemical and Physical Properties of Sodium Ionic Conductors for solid-state batteries*, **n.d.**
[10] A.K. Kuriakose, T.A. Wheat, A. Ahmad, J. Dirocco, *Synthesis, sintering, and microstructure of nasicons*, **n.d.**
[11] I.N. David, T. Thompson, J. Wolfenstine, J.L. Allen, J. Sakamoto, J. Am. Ceramic Soc. 98 (2015) 1209–1214.
[12] R. Murugan, V. Thangadurai, W. Weppner, Angew. Chemie Int. Ed. 46 (2007) 7778–7781.
[13] J.A.S. Oh, X. Xu, Z. Zeng, K. Wang, N.Y.J. Tan, E. Kok, J. Huang, L. Lu, Energy Environ. Mater. 6 (2023), https://doi.org/10.1002/eem2.12472.
[14] M. Rosen, M. Finsterbusch, O. Guillon, D. Fattakhova-Rohlfing, J. Mater. Chem. A Mater. 10 (2022) 2320–2326.
[15] E. Dashjav, M. Gellert, G. Yan, D. Grüner, N. Kaiser, S. Spannenberger, I. Kraleva, raul Bermejo, M.-T. Gerhards, Q. Ma, J. Malzbender, B. Roling, F. Tietz O. Guillon, *Microstructure, ionic conductivity and mechanical properties of tape-cast Li1.5Al0.5Ti1.5P3O12 electrolyte sheets*, **n.d.**
[16] A.C. Kutlu, D. Nötzel, C. Ziebert, H.J. Seifert, I. Ul Mohsin, *Batter Supercaps* 2023, DOI 10.1002/batt.202300357.
[17] A. Chen, C. Qu, Y. Shi, F. Shi, Front. Energy Res. 8 (2020), https://doi.org/10.3389/fenrg.2020.571440.
[18] A. Maurel, M. Haukka, E. MacDonald, L. Kivijärvi, E. Lahtinen, H. Kim, M. Armand, A. Cayla, A. Jamali, S. Grugeon, L. Dupont, S. Panier, Addit. Manuf. (2021) 37, https://doi.org/10.1016/j.addma.2020.101651.
[19] G.T. Hitz, D.W. McOwen, L. Zhang, Z. Ma, Z. Fu, Y. Wen, Y. Gong, J. Dai, T. R. Hamann, L. Hu, E.D. Wachsman, Mater. Today 22 (2019) 50–57.
[20] D. Checot-Moinard, C. Rigollet, P. Lourdin, Powder Technol. 208 (2011) 472–479.
[21] I. Calafel, R.H. Aguirresarobe, M.I. Peñas, A. Santamaria, M. Tierno, J.I. Conde, B. Pascual, Materials 13 (2020) 178.
[22] P. Thomas-Vielma, A. Cervera, B. Levenfeld, A. Várez, J. Eur. Ceram Soc. 28 (2008) 763–771.
[23] Z. Jiang, B. Diggle, M.L. Tan, J. Viktorova, C.W. Bennett, L.A. Connal, Adv. Sci. 7 (2020), https://doi.org/10.1002/advs.202001379.
[24] D. Nötzel, R. Eickhoff, T. Hanemann, Materials (2018) 11, https://doi.org/10.3390/ma11081463.
[25] Y. Tao, F. Kong, Z. Li, J. Zhang, X. Zhao, Q. Yin, D. Xing, P. Li, J. Mater. Res. Technol. 15 (2021) 4860–4879.
[26] S. Rolere, U. Soupremanien, M. Bohnke, M. Dalmasso, C. Delafosse, R. Laucournet, J. Mater. Process Technol. (2021) 295, https://doi.org/10.1016/j.jmatprotec.2021.117163.
[27] McEntire B.J., Bartlett R.A., Miller G.R., Gordon R.S., *The effect of decomposition on the densification and properties of NASICON ceramic electrolytes*, 1982.
[28] A.G. Jolley, G. Cohn, G.T. Hitz, E.D. Wachsman, Ionics 21 (2015) 3031–3038.
[29] S.K. Pal, R. Saha, G.V. Kumar, S. Omar, J. Phys. Chem. C 124 (2020) 9161–9169.
[30] K.-D. Kreuer, H. Kohler, J. Maier, *Sodium ion conductors with nasicon framework structure*, **n.d.**
[31] R.O. Fuentes, F.M. Figueiredo, F.M.B. Marques, J.I. Franco, *Influence of microstructure on the electrical properties of nasicon materials*, 2001.
[32] S. Naqash, D. Sebold, F. Tietz, O. Guillon, J. Am. Ceram. Soc. 102 (2019) 1057–1070.
[33] H. Salmang, H. Scholze, KERAMIK, Springer, Berlin Heidelberg, 2006.
[34] J.F. Valera-Jiménez, J.C. Pérez-Flores, M. Castro-García, J. Canales-Vázquez, Appl. Mater Today (2021) 25, https://doi.org/10.1016/j.apmt.2021.101243.
[35] A. Das, E.L. Gilmer, S. Biria, M.J. Bortner, ACS Appl. Polym Mater. 3 (2021) 1218–1249.
[36] S.J. Glass, K.G. Ewsuk, *Ceramic Powder Compact.*, **n.d.**
[37] D. Nötzel, T. Hanemann, Materials 13 (2020) 1–12.
[38] M.M. Rueda, M.C. Auscher, R. Fulchiron, T. Périé, G. Martin, P. Sonntag, P. Cassagnau, Prog. Polym Sci. 66 (2017) 22–53.
[39] Z. Zhang, Q. Zhang, J. Shi, Y.S. Chu, X. Yu, K. Xu, M. Ge, H. Yan, W. Li, L. Gu, Y. S. Hu, H. Li, X.Q. Yang, L. Chen, X. Huang, Adv. Energy Mater. 7 (2017), https://doi.org/10.1002/aenm.201601196.
[40] J. Luo, G. Zhao, W. Qiang, B. Huang, J. Am. Ceramic Soc. 105 (2022) 3428–3437.
[41] S. Naqash, Q. Ma, F. Tietz, O. Guillon, Solid State Ion 302 (2017) 83–91.
[42] S. Narayanan, S. Reid, S. Butler, V. Thangadurai, Solid State Ion. 331 (2019) 22–29.
[43] V. Ramar, S. Kumar, S.R. Sivakkumar, P. Balaya, Electrochim. Acta 271 (2018) 120–126.
[44] A.J.K. Tieu, E. Mahayoni, Y. Li, Z. Deng, F. Fauth, J.N. Chotard, V. Seznec, S. Adams, C. Masquelier, P. Canepa, J. Mater. Chem. A Mater. 11 (2023) 23233–23242.
[45] T. Fuchs, C.G. Haslam, F.H. Richter, J. Sakamoto, J. Janek, Adv. Energy Mater. (2023) 13, https://doi.org/10.1002/aenm.202302383.
[46] Y. Lu, C.Z. Zhao, H. Yuan, X.B. Cheng, J.Q. Huang, Q. Zhang, Adv. Funct. Mater. (2021) 31, https://doi.org/10.1002/adfm.202009925.
[47] J.A.S. Oh, Y. Wang, Q. Zeng, J. Sun, Q. Sun, M. Goh, B. Chua, K. Zeng, L. Lu, J. Colloid Interface Sci. 601 (2021) 418–426.
[48] J.K. Eckhardt, P.J. Klar, J. Janek, C. Heiliger, ACS Appl. Mater Interfaces 14 (2022) 35545–35554.
[49] R. Miao, C. Wang, D. Li, C. Sun, J. Li, H. Jin, Small (2022) 18, https://doi.org/10.1002/smll.202204487.
[50] Z. Gao, J. Yang, H. Yuan, H. Fu, Y. Li, Y. Li, T. Ferber, C. Guhl, H. Sun, W. Jaegermann, R. Hausbrand, Y. Huang, Chem. Mater. 32 (2020) 3970–3979.
[51] Q. Ma, T. Ortmann, A. Yang, D. Sebold, S. Burkhardt, M. Rohnke, F. Tietz, D. Fattakhova-Rohlfing, J. Janek, O. Guillon, Adv. Energy Mater. 12 (2022), https://doi.org/10.1002/aenm.202201680.
[52] D.Spencer Jolly, Z. Ning, J.E. Darnbrough, J. Kasemchainan, G.O. Hartley, P. Adamson, D.E.J. Armstrong, J. Marrow, P.G. Bruce, ACS Appl. Mater. Interfaces 12 (2020) 678–685.
[53] C.L. Tsai, T. Lan, C. Dellen, Y. Ling, Q. Ma, D. Fattakhova-Rohlfing, O. Guillon, F. Tietz, J. Power Sources (2020) 476, https://doi.org/10.1016/j.jpowsour.2020.228666.
[54] T. Ortmann, S. Burkhardt, J.K. Eckhardt, T. Fuchs, Z. Ding, J. Sann, M. Rohnke, Q. Ma, F. Tietz, D. Fattakhova-Rohlfing, C. Kübel, O. Guillon, C. Heiliger, J. Janek, Adv Energy Mater. 13 (2023), https://doi.org/10.1002/aenm.202202712.